Computational Materials Science 203 (2022) 111110

Contents lists available at ScienceDirect

Computational Materials Science

journal homepage: www.elsevier.com/locate/commatsci

Spin gapless semiconductors in antiferromagnetic monolayer HC_4N_3BN under strain

Pham Nam Phong [a,*], Huy-Viet Nguyen [b]

[a] School of Engineering Physics, Hanoi University of Science and Technology (HUST), 1 Dai Co Viet Road, Hanoi 100000, Viet Nam
[b] Institute of Physics, Vietnam Academy of Science and Technology (VAST), 10 Dao Tan Street, Hanoi 100000, Viet Nam

ARTICLE INFO

Keywords:
Spin gapless semiconductor
Antiferromagnet
Carbon nitride
Strain
Density functional

ABSTRACT

A density functional study is presented for HC_4N_3BN monolayer, which is triazine g-C_4N_3 tailored with H at its graphitic sites and B plus N at vacant sites, under uniaxial or biaxial in-plane strain. For moderate strains up to about ±8 percent, first-principles molecular dynamics simulations prove its thermal stability at room temperature and electronic structure calculations show the persistence of antiferromagnetic ground state of the system. The material undergoes magnetic transitions to ferro- and ferrimagnetic orders respectively at the critical biaxial strain of −8.3% and uniaxial strain of 7.8%. Interestingly, both transitions occur when the electronic structures of strained systems show the character of a spin gapless semiconductor. The combined effect of spin charge transfer and band shifting is proposed as a possible explanation for these transitions. Our finding on this monolayer signifies the importance of strain engineering in designing novel materials for antiferromagnetic spintronics.

1. Introduction

Spin gapless semiconductor (SGS), since its conceptual proposal [1] and experimental realization [2] as a new state of quantum matter, has received growing interest from both fundamental and applied research, particularly towards the next-generation of spintronic devices [3–5]. The electronic structure of SGS, featuring fully spin-polarized carriers with zero excitation energy, is unique in that it bridges the gap between half-metallic and magnetic semiconducting/gapless materials [2,5], two classes of spintronics materials [6–8]. Half-metal (HM), being metallic in one spin state while semiconducting in the other [9], and magnetic semiconductor (MS), being semiconducting but endowed with magnetism [6,7], possess novel features that have found essential applications in the field such as spin-polarized current generation and injection or spin filtering [8,10].

In the emerging sub-field of antiferromagnetic spintronics, antiferromagnets (AFMs) or fully compensated ferrimagnets (FCFs) and their magnetism are among the research focuses [11,12] thanks to their small stray fields—an advantage that makes them useful in targeted devices and applications [3,4,10,12]. The notable material sub-classes include HM-AFM [13], thin-film FCF [14], van der Waals AFM [15], and in particular monolayers of MS-AFM [16]. It is the distinctive electronic structures of these materials classes that allow one to tune the system from one state to another under external influences [4]. In a recent study, we have demonstrated that semiconducting ferromagnetism, in particular antiferromagnetism, can be induced into the half-metallic two-dimensional (2D) g-C_4N_3 lattice when tailored with H and 2*p* elements [17].

Strain engineering can be employed in tuning the band structure and other properties of 2D nanomaterials [18]. For graphitic carbon nitride materials family, strain engineering has been proven effective in regulating magnetism or causing related transitions [19–22]. In the quest for SGSs towards spintronic applications, we show in this work, by means of density-functional calculations, that under a suitable uniaxial or biaxial in-plane strain the antiferromagnetic monolayer HC_4N_3BN proposed in our recent study can be turned into a SGS. Details of this interesting finding will be presented in Section 3, after a brief summary of the computational procedure and technical details given in Section 2, together with other computation results demonstrating thermal stability of the material and its AFM character when the applied strain is below the critical values of about 8 %. Finally, such transitions will be clarified in a physicochemical picture of band shifting and charge transfer.

2. Computational methods

We have performed spin-polarized plane-wave DFT simulations with PBEsol and HSE functionals [23,24] using the Quantum ESPRESSO

* Corresponding author.
E-mail address: phong.phamnam@hust.edu.vn (P.N. Phong).

https://doi.org/10.1016/j.commatsci.2021.111110
Received 15 September 2021; Received in revised form 11 October 2021; Accepted 29 November 2021
Available online 22 December 2021

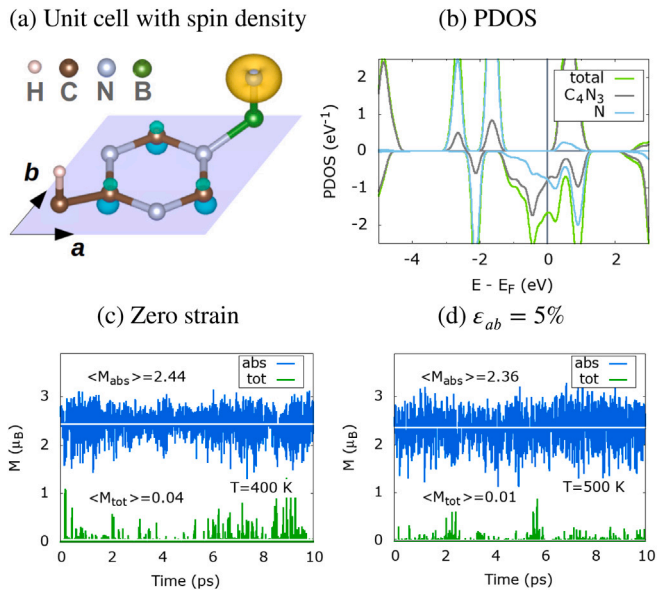

Fig. 1. The (1 × 1) unit cell with up/down spin density in yellow/cyan (a) and projected density of states (PDOS) of HC_4N_3BN monolayer (b). The fluctuation of magnetic moment per unit cell from first-principles molecular dynamics simulations without strain at 400 K (c) and with a biaxial strain ε_{ab} = 5% at 500 K (d). (For interpretation of the references to color in this figure legend, the reader is referred to the web version of this article.)

suite [25]. Optimized norm-conserving Vanderbilt pseudopotentials [26,27] and a kinetic energy cutoff of 80 Ry are chosen in calculations. The vacuum layer thickness of 19 Å is justified in simulating our 2D system. A (12 × 12) k-point grid with suitable smearing proves optimal to sample its Brillouin zone for (1 × 1) periodicity.

Unit cells are relaxed against the force and pressure thresholds set at 10^{-4} au and 1 kbar. All calculations with HSE hybrid functional have been carried out on top of PBEsol relaxed structures. A stochastic-velocity rescaling thermostat is used in Born Oppenheimer molecular dynamics simulations [28], the time-step Δt = 0.5 fs and relaxation times $\tau \approx 0.1$ ps. We use an implementation of the Bader analysis for partial atomic charge estimation [29]. Spin density plots are all rendered by VESTA program [30].

3. Results and discussion

HC_4N_3BN monolayer is regarded as a derivative of triazine g-C_4N_3 tailored with B at its vacant sites, N on-top of B, and H on-top of graphitic C sites, see Fig. 1(a) for the (1 × 1) unit cell of this material. Its lattice constant is 4.88 Å from structural relaxation using PBEsol functional. In this study, uniaxial and biaxial strains of magnitudes ε_b and ε_{ab} (the subscripts are used to indicate the types and directions of these strains, respectively) are applied along such two directions as shown by two lattice vectors $\boldsymbol{a}$ and $\boldsymbol{b}$ in the figure. Under these types of strain, a vector $\boldsymbol{v}^0$ transforms as $\boldsymbol{v} = (\mathbf{1} + \boldsymbol{\varepsilon})\cdot\boldsymbol{v}^0$, where the strain tensor $\boldsymbol{\varepsilon} = \mathrm{diag}(0, \varepsilon_b)$ for the former and $\boldsymbol{\varepsilon} = \mathrm{diag}(\varepsilon_{ab}, \varepsilon_{ab})$ for the latter. In our calculations, strains are introduced by varying the lattice vectors accordingly. Then, atomic positions in the unit cell are once again relaxed until all forces dropped below their preset threshold [21,22,31].

3.1. Strain-free properties and first-principles simulations

Fig. 1 presents electronic and magnetic properties of the system without strain. The projected density of states (PDOS) displayed in Fig. 1(b) shows clearly that the main contribution to the total PDOS is from N atoms at vacant sites and C_4N_3 ones, which constitute two sub-lattices of the material. Further analyzes (not presented here) pointed out that spin-down channels around the Fermi energy E_F are formed by N-$p_{x,y}$ and C-p_z orbitals of such two sub-lattices, respectively. The charges are about 1.3e for each spin channel, with opposite polarizations as can be seen in Fig. 1(a). Therefore, the total and absolute magnetization $M_{tot/abs}$, given as the integral of the spin density or its absolute value, are 0.0 and 2.6 μ_B per unit cell, respectively. This clearly signify HM-AFM character of the material, in contrasting to the pristine triazine g-C_4N_3, where its magnetic moment of 1 μ_B per unit cell is equally shared among three pyridinic N-sp^2 electrons [32].

To alleviate any fortuitous effects due to limitations of semi-local functionals, such as PBEsol, on the obtained results, we have performed the same analysis using the HSE hybrid functional, which is known to address electron correlations better, on top of PBEsol relaxed structures. HSE functional predicts $M_{tot/abs}$ approximately 0/3.6 μ_B. Charge transfer from B to such two opposite spin polarized sub-lattices N and C_4N_3 is the origin of this AFM character, on which both functionals agree. Bader charge analyzes show that all three valence electrons of B are transferred so, regardless of the functional used. Quantitatively, the spin charge transfer is stronger under hybrid functional usage, leading to the opening of a bandgap of 0.6 eV (see later in Fig. 3). It is this trait that renders the system a MS-FCF monolayer [17], which is among novel materials in antiferromagnetic spintronics.

Before going into details of interesting changes in electronic and magnetic properties of the system under strains, we present a brief checking on dynamical stability of the material by performing phonon calculations at the highly symmetric points of the Brillouin zone, namely Γ, K, and M. Our result agrees with the previous study [17], which reported no modes having imaginary frequencies therewith. In addition, we perform first-principles molecular dynamics simulations on thermal stability with a stochastic-velocity rescaling thermostat described in Section 2. Fig. 1(c, d) show the fluctuation of magnetic moment in such two simulations, one without strain and the other with biaxial strain ε_{ab} = 5%. The averaged temperatures over 10 ps are 407 K and 514 K versus their preset values of 400 K and 500 K, while $M_{tot/abs}$ averages are 0.04/2.44 and 0.01/2.36, respectively. Thus the monolayer and its antiferromagnetism are stable under such temperature and strain influences.

3.2. Strain-induced electronic and magnetic transitions

To see the electronic and magnetic transitions under strain in the system, we display in Fig. 2 the total and absolute magnetic moments as functions of biaxial or uniaxial strains, obtained with HSE functionals. Electronic characters in various strain regions showed in band structures are also indicated. For the case of uniaxial strain, no results are reported for compressive strains ε_b below −5% since the relaxation calculations did not converge within the preset criteria, which may signify certain structural instability; besides, similar results were obtained for the case of uniaxial strain along the a-axis, thus not presented afterwards.

Let us focus on three magnetic transitions marked with SGS in Fig. 2 and backed up with PDOS graphs in Fig. 3(b–d). The first one is a semiconductor-to-metal transition occurred at the critical strain ε_{ab} = −8.3%. Similar transitions were reported in literature, for instance, on strained ferromagnet (FM) silicene nanoribbons [31]. However, an interesting new result observed in our study is that there is also a magnetic transition from AFM to FM, see Fig. 2 and Table 1, whereas only FM trait was observed in the other. The second SGS state lies between those MS and HM ones of the system, where $\varepsilon_{ab} \approx 10\%$. This HM-to-MS electronic structure route has been explored in a recent study on g-C_4N_3 derived monolayers [17]. The third SGS state is somewhat unexpected, with ε_b = 7.8%, strangely situated between two all-MS regions. We note that such transitions were obtained under HSE hybrid functional usage, whereas PBEsol one predicts a metal/HM ground state of the systems in all strain regions. Electronic structure is presented in Fig. 3(b–d) for these three SGS configurations, alongside the other ones (e, f) under closely strained conditions for discussion. Apart from a spin-down band gap E_g = 0.6 eV, four graphs (a–d) there differ not significantly, all showing AFM character of the material (Table 1).

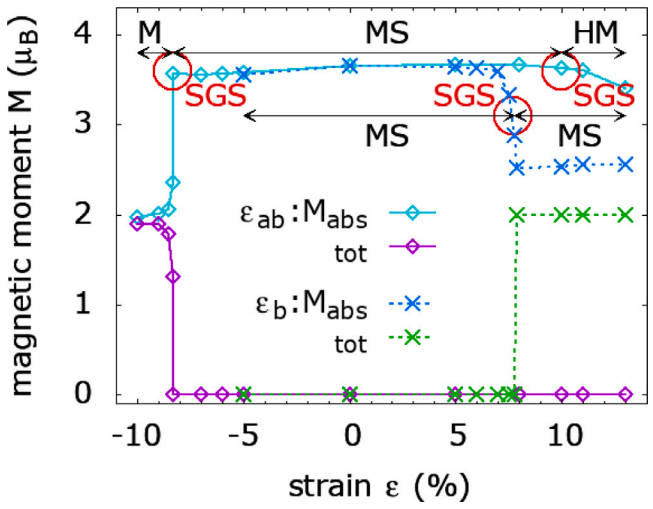

Fig. 2. Absolute and total magnetic moment vs. biaxial or uniaxial strain. Electronic structure character is noted in various strain regions as: M, HM, MS, and SGS for metal, half-metal, magnetic semiconductor, and spin gapless semiconductor.

Table 1
Characters (table footnotes) and magnetic moments (μ_B/unit cell) of the system at various strains, corresponding to PDOS graphs in Fig. 3. Three magnetic transitions at the critical strains are of SGS character, marked in Fig. 2.

Strain		Character[a]	M_{tot}	M_{abs}
Type	(%)			
	0	MS-AFM	0.0	3.6
ϵ_{ab}	10	SGS	0.0	3.6
ϵ_{ab}	−8.3	SGS	0.0	3.5
	−8.4	Metal-FM	1.8	2.1
ϵ_b	7.8	SGS	0.0	2.9
	7.9	MS-FI	2.0	2.5

AFM/FM/FI: Antiferromagnet/Ferromagnet/Ferrimagnet.
[a]MS/SGS: Magnetic/Spin gapless semiconductor.

3.3. Discussion

Under biaxial strain, there is simply a shift of the bands relative to E_F. Beyond a strain $\epsilon_{ab} \approx 10\%$, E_F is further shifted down, widening the HM (spin-flip) gap E_{sf} in Fig. 3(b), whereas the spin-down gap disappears, making our system a half-metal. The magnetic order, however, remains antiferromagnetic. Given the earlier charge transfer analysis, the favorable AFM ground state of our system and its HM characteristic are thus "interlocked", notwithstanding minor changes in the polarization, see Fig. 2. It is this trait that contrasts the MS to HM transition with the following one where we see drops in the magnetic moment.

Biaxial compression is also causing such a shift in electronic structure, however, with the reducing spin-flip gap in Fig. 3(c), which disappears for strains beyond $\epsilon_{ab} = -8.3\%$, unlike the previous scenario. Naturally our system turns metallic in this case, see Fig. 3(e). In addition, the deformation causes such an AFM/FM magnetic transition as in Fig. 2. The explanation lies in a fact that the precious HM characteristic is lost, hence both spin channels from C_4N_3 sub-lattice become occupied while the spin-up channel from N one being slightly altered.

The most noticeable outcome is with a transition under uniaxial strain at the critical value $\epsilon_b = 7.8\%$, see Figs. 2 and 3(d). This SGS state is found between two all-MS strain regions, and such a competing behavior was reported previously in a study on alloys between the MS and SGS configurations [33]. The transition occurs somehow to change our system from antiferromagnetic to ferrimagnetic, with $M_{tot/abs}$ values about 2.0/2.5. To give a physicochemical explanation

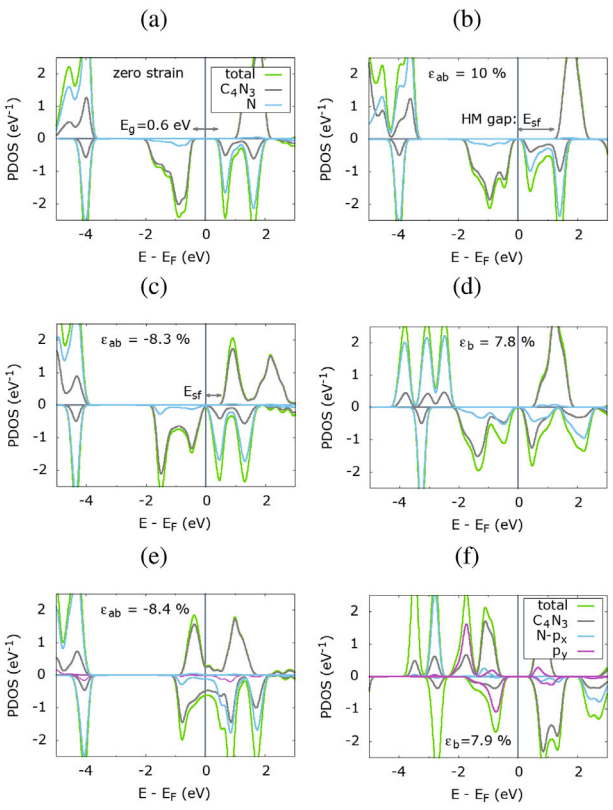

Fig. 3. PDOS using HSE hybrid functional, showing MS (a, f), SGS (b–d), and Metal (e) characters of the monolayer at respective strains.

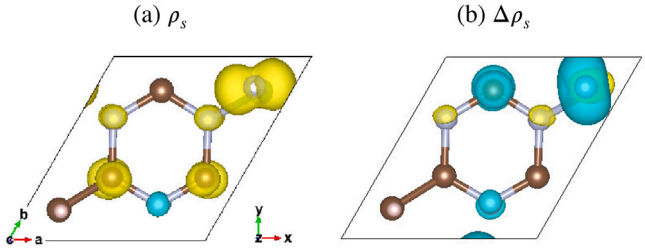

Fig. 4. The spin density ρ_s of the system (a) and polarization difference* (b) under uniaxial strain $\epsilon_b = 7.9\%$. Positive/negative values are in yellow/cyan, with the isosurface level 0.02. *$\Delta\rho_s = \rho_s(HC_4N_3BN) - \rho_s(HC_4N_3B) - \rho_s(N)$. (For interpretation of the references to color in this figure legend, the reader is referred to the web version of this article.)

for this transition, we present the results with $\epsilon_b = 7.9\%$ just above the critical value in Figs. 4 and 3(f) as follows.

On the one hand, note a new trait in the PDOS, where the peak around −1 eV from C_4N_3 sub-lattice of our relaxed system is no longer fully spin-down polarized. Specifically, the spin-down charge equally distributed in three C-p_z orbitals of C_4N_3 sub-lattice now turns spin-up polarized. Furthermore, their distribution becomes asymmetric due to uniaxial strain, see the spin density ρ_s in Fig. 4(a).

On the other hand, the deformation also breaks the symmetry between N-p_x and -p_y channels, see Fig. 3(f), leaving only the former contributed to the total spin density. Naturally, upon increasing the strain, N-p_y orbital is split from -p_x one around −4 eV, shifting up in energy while its anti-bonding orbital around 1 eV shifts down below E_F, in other words the polarization of N-p_y orbital due to the charge transfer, from B to N and C_4N_3 sub-lattices as reported, is eventually removed. This picture is further clarified with the so-called spin density difference defined as $\Delta\rho_s = \rho_s(HC_4N_3BN) - \rho_s(HC_4N_3B) - \rho_s(N)$, the

difference between polarizations of the system and its sub-lattices in Fig. 4(b). The positive/negative values of $\Delta\rho_s$ are rendered in yellow/cyan colors there, similar for the up/down polarization in other spin density ρ_s plots elsewhere. Here we clearly see that removal of the N-p_y orbital polarization.

4. Conclusion

In this study, we have reported the spin gapless semiconducting states in a novel monolayer namely HC_4N_3BN, designed from triazine g-C_4N_3 with H, B, and N, under uniaxial or biaxial strain. For strains below ±8 percent, the material possesses an antiferromagnetic ground state, its thermal stability at 400 K is confirmed in first-principles molecular dynamics simulations. The system undergoes magnetic transitions to a ferromagnetic order at the biaxial strain −8.3%, and to a ferrimagnetic order at the uniaxial strain 7.8%, while its antiferromagnetism survives in another transition at the biaxial strain ≈ 10%. SGS character is observed in the electronic structures of all these strained configurations, and such transitions are interpreted with a physicochemical picture as the combined effect of spin charge transfer and band shifting.

Our study is an effort searching for SGSs in the graphitic carbon nitride based materials [34], which are among p-state type SGS candidates in spintronics [3–5]. The other promising materials classes are ranging from the traditional bulk ones [35] to monolayers [36]. Since the electronic structure of such gapless materials is sensitive to external influences [1,2], that must be taken into account in designing novel spintronic materials. Spin gapless states could exist in between semiconducting and (half-)metallic ones [1], or in certain cases their coexistence in the material is hinted from both experimental and theoretical findings [33]. In addition, SGS character may also be found among the magnetic semiconducting configurations as demonstrated in this study. Thus our results signify the importance of strain engineering in searching for SGSs particularly in novel monolayers towards spintronic applications.

CRediT authorship contribution statement

Pham Nam Phong: Conceptualization, Methodology, Software, Validation, Investigation, Formal analysis, Visualization, Writing – original draft, Writing – review & editing. **Huy-Viet Nguyen:** Conceptualization, Methodology, Software, Validation, Investigation, Formal analysis, Resources, Writing – review & editing.

Declaration of competing interest

The authors declare that they have no known competing financial interests or personal relationships that could have appeared to influence the work reported in this paper.

Data availability

Section 2 has described in detail the material and methods. Standard modelings and simulations are available in the Quantum ESPRESSO open-source chemistry package.

Acknowledgment

Computational support to our project is from *tcp.iop* and *hpc.vast* cluster facilities (VAST). This research is funded by Vietnam National Foundation for Science and Technology Development (NAFOSTED) under grant number 103.01-2017.359.

References

[1] X.L. Wang, Proposal for a new class of materials: Spin gapless semiconductors, Phys. Rev. Lett. 100 (2008) 156404, http://dx.doi.org/10.1103/PhysRevLett.100.156404, URL: https://link.aps.org/doi/10.1103/PhysRevLett.100.156404.

[2] S. Ouardi, G.H. Fecher, C. Felser, J. Kübler, Realization of spin gapless semiconductors: The Heusler compound mn_2coal, Phys. Rev. Lett. 110 (2013) 100401, URL: https://link.aps.org/doi/10.1103/PhysRevLett.110.100401.

[3] X. Wang, Z. Cheng, G. Zhang, H. Yuan, H. Chen, X.-L. Wang, Spin-gapless semiconductors for future spintronics and electronics, Phys. Rep. 888 (2020) 1–57, http://dx.doi.org/10.1016/j.physrep.2020.08.004, URL: https://www.sciencedirect.com/science/article/pii/S037015732030291X.

[4] D. Rani, L. Bainsla, A. Alam, K.G. Suresh, Spin-gapless semiconductors: Fundamental and applied aspects, J. Appl. Phys. 128 (22) (2020) 220902, http://dx.doi.org/10.1063/5.0028918.

[5] Z. Yue, Z. Li, L. Sang, X. Wang, Spin-gapless semiconductors, Small 16 (31) (2020) 1905155, http://dx.doi.org/10.1002/smll.201905155, URL: https://onlinelibrary.wiley.com/doi/abs/10.1002/smll.201905155.

[6] C. Felser, G. Fecher, B. Balke, Spintronics: A challenge for materials science and solid-state chemistry, Angew. Chem. Int. Edn 46 (5) (2007) 668–699, http://dx.doi.org/10.1002/anie.200601815.

[7] S.A. Wolf, D.D. Awschalom, R.A. Buhrman, J.M. Daughton, S. von Molnár, M.L. Roukes, A.Y. Chtchelkanova, D.M. Treger, Spintronics: A spin-based electronics vision for the future, Science 294 (5546) (2001) 1488–1495, http://dx.doi.org/10.1126/science.1065389, URL: http://science.sciencemag.org/content/294/5546/1488.

[8] I. Žutić, J. Fabian, S. Das Sarma, Spintronics: Fundamentals and applications, Rev. Modern Phys. 76 (2004) 323–410, http://dx.doi.org/10.1103/RevModPhys.76.323, URL: https://link.aps.org/doi/10.1103/RevModPhys.76.323.

[9] M.I. Katsnelson, V.Y. Irkhin, L. Chioncel, A.I. Lichtenstein, R.A. de Groot, Half-metallic ferromagnets: From band structure to many-body effects, Rev. Modern Phys. 80 (2008) 315–378, http://dx.doi.org/10.1103/RevModPhys.80.315, URL: https://link.aps.org/doi/10.1103/RevModPhys.80.315.

[10] A. Hirohata, K. Takanashi, Future perspectives for spintronic devices, J. Phys. D. Appl. Phys. 47 (19) (2014) 193001, URL: http://stacks.iop.org/0022-3727/47/i=19/a=193001.

[11] V. Baltz, A. Manchon, M. Tsoi, T. Moriyama, T. Ono, Y. Tserkovnyak, Antiferromagnetic spintronics, Rev. Modern Phys. 90 (1) (2018) 015005, http://dx.doi.org/10.1103/revmodphys.90.015005.

[12] T. Jungwirth, X. Marti, P. Wadley, J. Wunderlich, Antiferromagnetic spintronics, Nat. Nanotechnol. 11 (3) (2016) 231–241, http://dx.doi.org/10.1038/nnano.2016.18.

[13] X. Hu, Half-metallic antiferromagnet as a prospective material for spintronics, Adv. Mater. 24 (2) (2012) 294–298, http://dx.doi.org/10.1002/adma.201102555, URL: https://onlinelibrary.wiley.com/doi/abs/10.1002/adma.201102555.

[14] R. Sahoo, et al., Compensated ferrimagnetic tetragonal Heusler thin films for antiferromagnetic spintronics, Adv. Mater. 28 (38) (2016) 8499–8504, http://dx.doi.org/10.1002/adma.201602963, URL: https://onlinelibrary.wiley.com/doi/abs/10.1002/adma.201602963.

[15] N. Miao, B. Xu, L. Zhu, J. Zhou, Z. Sun, 2D intrinsic ferromagnets from van der waals antiferromagnets, J. Am. Chem. Soc. 140 (7) (2018) 2417–2420, http://dx.doi.org/10.1021/jacs.7b12976.

[16] B. Xu, J. Yin, Y.D. Xia, X.G. Wan, Z.G. Liu, Ferromagnetic and antiferromagnetic properties of the semihydrogenated SiC sheet, Appl. Phys. Lett. 96 (14) (2010) 143111, http://dx.doi.org/10.1063/1.3379025.

[17] P.N. Phong, N.T. Ngoc, P.T. Lam, M.-T. Nguyen, H.-V. Nguyen, From half-metallic to magnetic semiconducting triazine g-C_4N_3: computational designs and insight, RSC Adv. 11 (2021) 38944, http://dx.doi.org/10.1039/D1RA05348E.

[18] C. Tan, et al., Recent advances in ultrathin two-dimensional nanomaterials, Chem. Rev. 117 (9) (2017) 6225–6331, http://dx.doi.org/10.1021/acs.chemrev.6b00558.

[19] L.Z. Liu, X.L. Wu, X.X. Liu, P.K. Chu, Electronic structure and magnetism in g-c_4n_3 controlled by strain engineering, Appl. Phys. Lett. 106 (13) (2015) 132406, http://dx.doi.org/10.1063/1.4916814.

[20] X. Zhang, M. Zhao, A. Wang, X. Wang, A. Du, Spin-polarization and ferromagnetism of graphitic carbon nitride materials, J. Mater. Chem. C 1 (39) (2013) 6265, http://dx.doi.org/10.1039/c3tc31213e.

[21] X. Li, S. Zhang, Q. Wang, Stability and physical properties of a tri-ring based porous g-C_4N_3 sheet, Phys. Chem. Chem. Phys. 15 (19) (2013) 7142, http://dx.doi.org/10.1039/c3cp44660c.

[22] X. Li, J. Zhou, Q. Wang, Y. Kawazoe, P. Jena, Patterning graphitic C–N sheets into a kagome lattice for magnetic materials, J. Phys. Chem. Lett. 4 (2) (2012) 259–263, http://dx.doi.org/10.1021/jz3018804.

[23] J.P. Perdew, A. Ruzsinszky, G.I. Csonka, O.A. Vydrov, G.E. Scuseria, L.A. Constantin, X. Zhou, K. Burke, Restoring the density-gradient expansion for exchange in solids and surfaces, Phys. Rev. Lett. 100 (2008) 136406, http://dx.doi.org/10.1103/PhysRevLett.100.136406, URL: https://link.aps.org/doi/10.1103/PhysRevLett.100.136406.

[24] J. Heyd, G.E. Scuseria, M. Ernzerhof, Erratum: ‘‘Hybrid functionals based on a screened Coulomb potential’’, J. Chem. Phys. 124 (21) (2006) 219906, http://dx.doi.org/10.1063/1.2204597; J. Chem. Phys 118 (2003) 8207.

[25] P. Giannozzi, et al., Advanced capabilities for materials modelling with quantum ESPRESSO, J. Phys.: Condens. Matter 29 (46) (2017) 465901, URL: http://stacks.iop.org/0953-8984/29/i=46/a=465901, http://www.quantum-espresso.org.

[26] D.R. Hamann, Optimized norm-conserving vanderbilt pseudopotentials, Phys. Rev. B 88 (2013) 085117, http://dx.doi.org/10.1103/PhysRevB.88.085117, URL: https://link.aps.org/doi/10.1103/PhysRevB.88.085117.

[27] M. Schlipf, F. Gygi, Optimization algorithm for the generation of ONCV pseudopotentials, Comput. Phys. Comm. (ISSN: 0010-4655) 196 (2015) 36, http://dx.doi.org/10.1016/j.cpc.2015.05.011, URL: http://www.sciencedirect.com/science/article/pii/S0010465515001897.

[28] G. Bussi, D. Donadio, M. Parrinello, Canonical sampling through velocity rescaling, J. Chem. Phys. 126 (1) (2007) 014101, http://dx.doi.org/10.1063/1.2408420.

[29] W. Tang, E. Sanville, G. Henkelman, A grid-based bader analysis algorithm without lattice bias, J. Phys.: Condens. Matter 21 (8) (2009) 084204, URL: http://stacks.iop.org/0953-8984/21/i=8/a=084204, http://theory.cm.utexas.edu/bader/.

[30] K. Momma, F. Izumi, VESTA3 for three-dimensional visualization of crystal, volumetric and morphology data, J. Appl. Cryst. 44 (6) (2011) 1272–1276, http://dx.doi.org/10.1107/S0021889811038970.

[31] Y. Ding, Y. Wang, Electronic structures of zigzag silicene nanoribbons with asymmetric sp^2–sp^3 edges, Appl. Phys. Lett. 102 (14) (2013) 143115, http://dx.doi.org/10.1063/1.4801948.

[32] A. Du, S. Sanvito, S.C. Smith, First-principles prediction of metal-free magnetism and intrinsic half-metallicity in graphitic carbon nitride, Phys. Rev. Lett. 108 (2012) 197207, URL: https://link.aps.org/doi/10.1103/PhysRevLett.108.197207.

[33] Y. Venkateswara, S. Gupta, S.S. Samatham, M.R. Varma, Enamullah, K.G. Suresh, A. Alam, Competing magnetic and spin-gapless semiconducting behavior in fully compensated ferrimagnetic CrVTiAl: Theory and experiment, Phys. Rev. B 97 (5) (2018) 054407, http://dx.doi.org/10.1103/physrevb.97.054407.

[34] X. Zhang, A. Wang, M. Zhao, Spin-gapless semiconducting graphitic carbon nitrides: A theoretical design from first principles, Carbon 84 (2015) 1–8, http://dx.doi.org/10.1016/j.carbon.2014.11.049.

[35] X. Wang, Z. Cheng, J. Wang, X.-L. Wang, G. Liu, Recent advances in the Heusler based spin-gapless semiconductors, J. Mater. Chem. C 4 (30) (2016) 7176–7192, http://dx.doi.org/10.1039/c6tc01343k.

[36] G. Gao, G. Ding, J. Li, K. Yao, M. Wu, M. Qian, Monolayer mxenes: promising half-metals and spin gapless semiconductors, Nanoscale 8 (16) (2016) 8986–8994, http://dx.doi.org/10.1039/c6nr01333c.